AIAA 2001-2155

Time-Accurate Simulations and Acoustic Analysis of Slat Free-Shear Layer

Mehdi R. Khorrami
Bart A. Singer
NASA Langley Research Center
Hampton, VA 23681-2199

Mert E. Berkman
High Technology Corporation
28 Research Drive
Hampton, VA 23666

7th AIAA/CEAS Aeroacoustics Conference
28--30 May, 2001, Maastricht, Netherlands

TIME-ACCURATE SIMULATIONS AND ACOUSTIC ANALYSIS OF SLAT FREE-SHEAR LAYER

Mehdi R. Khorrami*
Bart A. Singer†
NASA Langley Research Center
Hampton, VA 23681-2199

Mert E. Berkman‡
High Technology Corporation
28 Research Drive
Hampton, VA 23666

A detailed computational aeroacoustic analysis of a high-lift flow field is performed. Time-accurate Reynolds Averaged Navier-Stokes (RANS) computations simulate the free shear layer that originates from the slat cusp. Both unforced and forced cases are studied. Preliminary results show that the shear layer is a good amplifier of disturbances in the low- to mid-frequency range. The Ffowcs-Williams and Hawkings equation is solved to determine the acoustic field using the unsteady flow data from the RANS calculations. The noise radiated from the excited shear layer has a spectral shape qualitatively similar to that obtained from measurements in a corresponding experimental study of the high-lift system.

Introduction

As part of a major effort to reduce aircraft noise emission, airframe noise has received renewed attention in the past few years.[1] To develop viable noise reduction technologies, a concerted effort toward isolating and understanding noise sources associated with individual components of a high-lift system has been undertaken. Experimental studies by Hayes et al.,[2] Dobrzynski et al.,[3] Davy and Remy,[4] Grosche et al.,[5] Michel et al.,[6] Storms et al.,[7] and Olson et al.,[8] along with the in-house measurements at NASA Langley Research Center (LaRC), clearly show the importance of a leading-edge slat as a major contributor to overall airframe noise. The LaRC tests, which are the focus of our attention, involved a generic Energy Efficient Transport (EET) high-lift model. The model is comprised of a slat, a main element, and a flap (fig. 1). Both aerodynamic and acoustic measurements were obtained in the Low Turbulence Pressure Tunnel (LTPT) during entries in 1998 and 1999.

In the present paper we continue studying noise sources associated with a leading-edge slat in a high-lift setting. Our previous research focused on accurate unsteady simulations of the slat trailing-edge flow field and computation of the resulting acoustic far field.[9,10] Current research applies the framework established in references 9 and 10 to the free shear layer that originates at the slat cusp.

In the experiments, acoustic measurements were made by a team from Boeing Commercial Airplane Company using the Boeing microphone-array technique. The array was mounted roughly one meter from the underside of the model. The setting for the baseline case consisted of a main element angle of attack that varied between 6 to 10 degrees, a flap deflection angle of 30 degrees, and a slat deflection angle of 30 degrees. For the angles of attack considered, with the exception of minor details, the EET slat produces acoustic signatures that have similar features.

Representative microphone-array measurements for a 9-degree case from the 1999 entry are shown in figure 2. The plotted spectra are in $1/12^{th}$-octave bands. The high-frequency microphone array had a smaller aperture than the low-frequency array and was better suited for resolving high-frequency noise. The flow Mach number is 0.2, corresponding to a typical approach condition. Two prominent features

*Research Scientist formally with High Technology Corp. Senior Member AIAA.

†Assistant Branch Head, Computational Modeling and Simulation Branch. Member AIAA.

‡Research Scientist; currently with ArvinMeritor Exhaust Systems, Member AIAA.

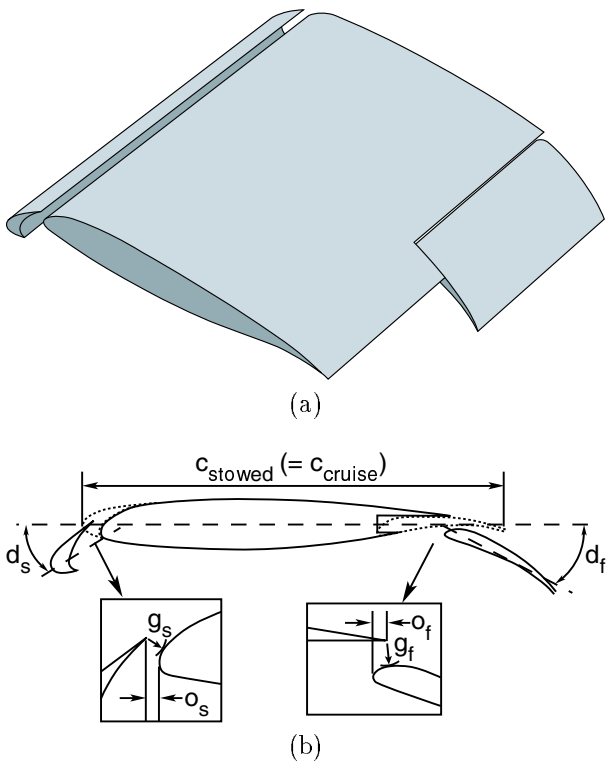

Figure 1. Three-element EET high-lift system. (a) Three-dimensional model. (b) Cross-sectional view.

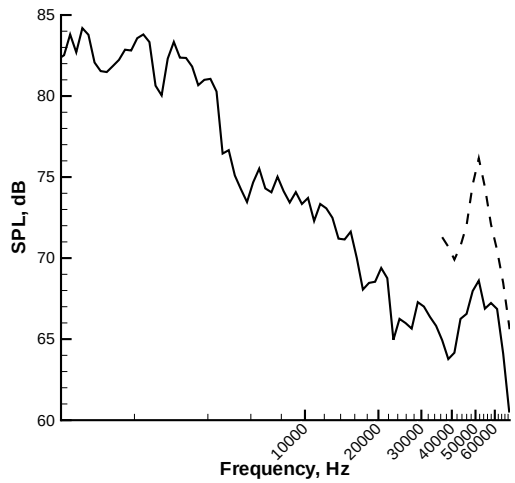

Figure 2. Measured acoustic spectrum for slat in $1/12^{th}$-octave bands. Test parameters are: slat deflection angle of 30 degrees, main element angle of attack of 9 degrees, flap deflection angle of 30 degrees, Mach number of 0.2, Reynolds number of 7.5 million. ——— low-frequency microphone array, – – – – – high-frequency microphone array.

in the acoustic spectrum are a relatively high amplitude peak near 50,000 Hz and high sound levels in the lower frequency range that drop abruptly between 4,000 Hz to 5,000 Hz.

Our previous efforts,[9,10] proved our first conjecture that vortex shedding at the slat blunt trailing-edge is the mechanism responsible for the tonal peak in the acoustic spectra at high frequencies. During the course of that study, our time-accurate solution pointed to the presence of additional flow oscillations in the slat-cove region. The observed oscillations were associated with the slat free shear layer and had frequencies between 2,000 Hz and 4,000 Hz.

This early simulation[9] also suggested that the shear layer may self-excite and would not require explicit forcing. Therefore, our preliminary time-accurate simulations involved no forcing at the slat cusp, relying instead on the presence of numerical perturbations in the initial solution to provide necessary excitation for the cove shear layer. Initially this natural forcing was adequate, as the shear layer self-excited in the proper frequency band. Unfortunately, the excitation did not last more than a few periods before numerical dissipation damped the shear layer instability modes and caused the flow field to return toward its original quasi-steady state.

Lack of sustained disturbance growth prompted us to undertake a more thorough study. In this effort we focused our attention on the role of large-scale instabiliy modes of the slat shear layer in generating noise. Therefore, goals of the present study are to test our conjecture that amplified perturbations in the free shear-layer are responsible for low-frequency content of the acoustic spectra. While similar conjectures have been put forth by other investigators (Dobrzynski et al.[3]), the issue remains unresolved. Although our current simulations were started in late 1998 and early 1999, two recent studies lend added support to our conjecture. Using Particle Image Velocimetry (PIV), Paschal et al.[11] were able to map the flow field slightly downstream of the slat trailing edge. At low angles of attack (4 degrees), the PIV-generated images show the presence of large, strong spanwise vortices in the slat's wake. Size and location of these rollers, relative to the wake, preclude the slat trailing edge as the source. In all likelihood, as pointed out by Paschal et al., these vortices originate from the slat-cove region and then are pumped through the gap. As the angle of attack is increased, unsteadiness coming out of the cove is diminished and the number of vortices in the wake is reduced significantly. Similarly, Takeda et al.[12] employed the PIV technique to map the flow field inside a slat-cove area. Growth of the shear-layer dis-

turbances and their subsequent evolution into large-scale structures are captured.

Computational Approach

The computational framework employed in the present study was explained in detail in references 9 and 10. Only a brief overview is given below.

As in reference 9, the CFL3D solver is used to perform time-accurate flow-field simulations. CFL3D is a finite-volume formulation-based code that solves time-dependent compressible thin-layer Navier-Stokes equations. CFL3D offers a wide variety of turbulence models, including 0-, 1-, and 2-equation models. Based on our past experience, the 2-equation SST (k-ω) Menter[13] model is selected and preferred for the present problem.

All current computations are performed using the second-order-accurate time discretization and the "dual time stepping" method. Thirty subiterations, in conjunction with 3-level V-type multigrid cycles, are utilized to ensure approximately two orders of magnitude drop in both mean-flow and turbulence-model residuals during each time step.

A full account of the three-element high-lift EET model and grid construction has been given by Khorrami et al.[9] For the present work, it suffices to mention that in the stowed position, the model has a chord of 21.65 inches (0.55 m) with slat and flap chords of 15 percent and 30 percent, respectively. The geometrical settings associated with the slat and flap (gaps g_s and g_f; overhangs o_s and o_f) in the baseline experiment are provided in table 1 where the distances are given as a percentage of the stowed chord. A graphical representation of the respective gaps and overhangs are shown in figure 1b. In the 1998 entry, angle of attack for the baseline experiment was set at 10 degrees and the deployed flap was part span. To match loading on the slat and the main element, present two-dimensional (2D) simulations are performed at 8 degrees angle of attack. In the 1999 entry, the part-span flap was replaced by a full-span flap with a slightly different profile. The slat gap and overhang remained identical. The new flap had little effect on relevant features of the measured acoustic spectra. Therefore, current simulations, which are conducted using the original flap profile, apply to both 1998 and 1999 experiments.

The present grid is identical to the "refined grid" employed in reference 9. The 2D grid has 21 blocks and approximately 433 K total nodes. More than 60 percent of the points are clustered in regions surrounding the slat and leading edge of the main element. To illustrate this point, mesh distribution in the slat's vicinity is shown in figure 3. For clarity, every other point is displayed. Notice that mesh clustering occurs at the solid surfaces, trailing edge, wake, and the cove. Deliberate concentration of mesh points in the slat cove region helps ensure accurately capturing the free shear layer that forms at the slat-cusp region tip.

Slat angle, δ_s	30 deg
Flap angle, δ_f	30 deg
Slat gap, g_s	2.44%
Flap gap, g_f	3.0%
Slat overhang, o_s	-1.52%
Flap overhang, o_f	1.7%

Table 1. Geometrical Settings

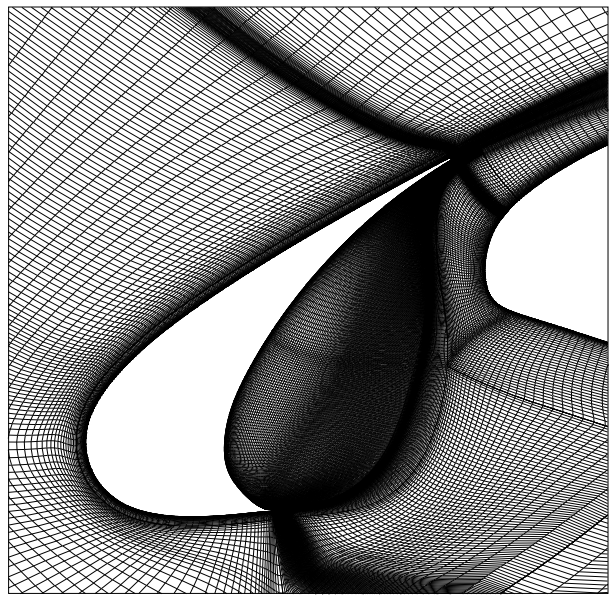

Figure 3. Grid distribution in vicinity of slat. Every other point is shown.

Forcing Strategy

As discussed in the introduction section and based on our previous simulations, a decision was made to introduce low levels of forcing into the flow field. Controlled forcing helps to isolate and capture the mechanism(s) responsible for low frequency oscillations observed in the slat cove region. After careful consideration, the most appropriate forcing location was selected on the slat bottom surface, roughly two to three local boundary layer heights upstream of the finite thickness cusp (fig. 4). The forced quantity is the vertical velocity, which at the forcing location, closely approximates wall-normal velocity. A simple harmonic function given by equations (1) and (2) was chosen to represent the forcing function where t

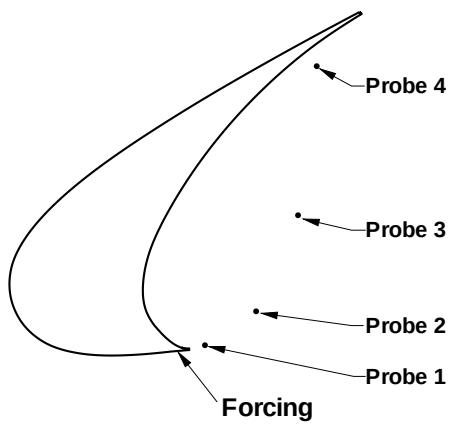

Figure 4. Location of forcing and computational probes.

and x denote time and streamwise direction, respectively.

$$g(x,t) = \frac{A_0}{N} h(x) \sum_{i=1}^{N} \sin(\Omega_i t + \psi_i) \tag{1}$$

$$h(x) = 1 - b_1 (x - b_2)^2 \tag{2}$$

In equation (1), the summation is over N equally spaced frequency bins, each with a center frequency Ω_i that differs by 93 Hz. To ensure the independence of individual frequencies, a randomly generated phase, ψ_i, is assigned to each bin. Also note that in order to avoid forcing at a single point, amplitude of the source is distributed over several grid nodes (seven in the present case) using a parabolic variation in x. The constants b_1 and b_2 are chosen to ensure zero velocity at the edges of the forcing region. Finally, A_0 represents the root mean square (rms) of the signal and is used to set desired amplitude levels.

The time consuming nature of the unsteady simulations and the need to generate meaningful time records limited the number of cases computed. The present set of computations is focused on flow fields forced over two different frequency bands. The first simulation involves frequency band 1,200 Hz $< f <$ 5,000 Hz corresponding to the observed range of frequencies of interest in the measured spectra. Once it became clear (from the simulated flow field) that the shear layer is an efficient amplifier of disturbances in the observed frequency range, frequency of the forcing function was expanded to encompass a range approximately twice that of the initial distribution. For the second simulation, the selected frequency band is 700 Hz $< f <$ 10,000 Hz. Widening the frequency band was significant for two related reasons. Given the shear layer's thinness near the cusp, a wider frequency band allows a more natural selection process for the most amplified disturbances. In addition, it removes any ambiguity regarding the effect of initial forcing distribution on the final outcome of the established flow field. We must also mention that for both cases, the rms amplitude A_0 is fixed at 3 percent of the freestream velocity.

Acoustic Procedure

Previously, Singer et al.[10,14] explored the use of unsteady computational results in acoustic-propagation codes based on the Ffowcs Williams and Hawkings[15] (hereafter referred to as FW-H) equation. Such codes compute the acoustic signal at a distant observer position by integrating the FW-H equation. Following Brentner and Farassat,[16] the FW–H equation may be written in differential form as

$$\Box^2 p'(\mathbf{x},t) = \frac{\partial^2}{\partial x_i \partial x_j}[T_{ij} H(f)] - \frac{\partial}{\partial x_i}[L_i \delta(f)] + \frac{\partial}{\partial t}[(\rho_0 U_n)\delta(f)] \tag{3}$$

where $\Box^2 \equiv \frac{1}{c^2}\frac{\partial^2}{\partial t^2} - \nabla^2$ is the wave operator, c is ambient speed of sound, t is observer time, p' is acoustic pressure, ρ' is perturbation density, ρ_0 is free-stream density, $f = 0$ describes the data surface, $\delta(f)$ is the Dirac delta function, and $H(f)$ is the Heaviside function. The quantities U_i and L_i are defined as

$$U_i = (1 - \frac{\rho}{\rho_0}) v_i + \frac{\rho u_i}{\rho_0} \tag{4}$$

and

$$L_i = P_{ij} \hat{n}_j + \rho u_i (u_n - v_n) \tag{5}$$

respectively. In the above equations, ρ is total density, ρu_i is momentum in the i direction, v_i is velocity of the data surface $f = 0$, and P_{ij} is the compressive stress tensor. For an inviscid fluid, $P_{ij} = p\delta_{ij}$ where p is the perturbation pressure and δ_{ij} is the Kronecker delta. The subscript n indicates projection of a vector quantity in the surface-normal direction. To obtain a solution to equation (3), the first term on the right-hand-side must be integrated over the volume outside data surface $f = 0$ wherever Lighthill stress tensor T_{ij} is nonzero in this region. In the work reported here, this term is neglected; however, the main effects of nonzero T_{ij} within the flow can

be included by choosing a data surface containing all the volume with significant T_{ij} contributions.

The other terms on the right-hand-side of equation (3) include those determined by unsteady flow field on the data surface. Provided that the unsteady flow on data surface $f = 0$ is correct, reference 14 demonstrates that the FW-H equation correctly propagates the acoustic radiation from several source regions, including complex signals associated with acoustic scattering from sharp edges. Reference 10 demonstrates use of the FW-H equation to propagate noise generated at the trailing edge of a slat.

Here only the 2D version of the FW-H equation is used to predict the sound field. We use an extremely efficient code developed by Lockard[17] for computing the 2D acoustic field from 2D CFD data. The code performs computation in the frequency domain; hence, unsteady CFD data must be transformed from the time domain.

Transformation involves first removing initial transient data from the CFD calculation. Then, the data record is divided into segments of 4,096 time steps with the latter 2,048 time steps of each record being incorporated into the subsequent segment. A modified Hanning window is applied to each data segment. The modified Hanning window includes a standard Hanning filter for the first and last 12.5 percent of the data, and a boxcar filter for the middle 75 percent. Windowed data is scaled to preserve the original energy in the signal and then Fourier-transformed into the frequency domain. The data segments introduce an artificial periodicity of 366 Hz, but this frequency is far lower than the frequencies of interest in this flow. The spectra obtained with each of the 4,096 time steps are then averaged to smooth the spectrum.

All acoustic calculations are performed for observers located a fixed distance from the slat's trailing edge. The fixed distance corresponds closely to the distance from the slat trailing edge to the wind-tunnel ceiling. Directivity angles are indicated in figure 5; zero degrees is in the downstream direction, 270 degrees is groundward in normal flight, but toward the microphone array in the wind tunnel.

Another important issue involves the choice of data surface for the FW-H calculation. In this work the three data surfaces used are illustrated in figure 6.

Figure 6 shows the upstream portion of data surfaces used for the FW-H calculations reported here. Figure 6(a) shows the upstream portion of the "on-body data surface." This data surface is coincident with the slat and main element bodies. Figure 6(b) shows the upstream portion of the "standard off-body data surface." This data surface extends outside the boundary layer of high-lift elements and encompasses the slat-cove region. Figure 6(c) shows a "modified off-body data surface." The modified off-body data surface is the same as the standard off-body data surface over the dashed-line region; however, over the solid-line region (essentially the slat's suction surface), the modified off-body data surface uses the on-body grid and data. Reasons for use of the modified data surface will be discussed later.

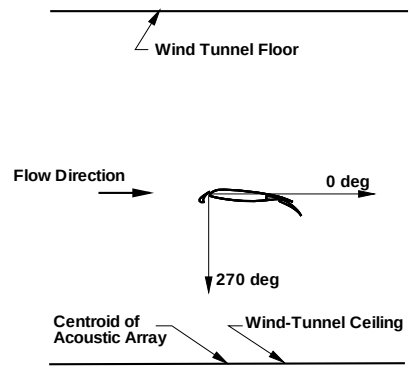

Figure 5. Schematic of model in wind tunnel. Flow from left to right. Acoustic directivity angles 0 and 270 degrees are indicated. View is rotated relative to experimental setup.

Results

RANS Simulations

Computations and postprocessing of the results are carried out in a non-dimensional fashion. The non-dimensionalization is with respect to a reference length (stowed chord), a reference speed of sound (a_∞), a reference density (ρ_∞), and a reference kinematic viscosity (ν_∞). For the present case, reference flow variables were set to match conditions at the LTPT test section entrance. Computations are done in a fully-turbulent mode using the two equation k-ω turbulence model. Unless indicated otherwise, all simulations are obtained for M = 0.2 and Re = 7.2×10^6.

A constant nondimensional time step of $\Delta t = 4.116 \times 10^{-4}$ (corresponding to 200 points per period for a 7,500 Hz signal) is used for all simulations. The

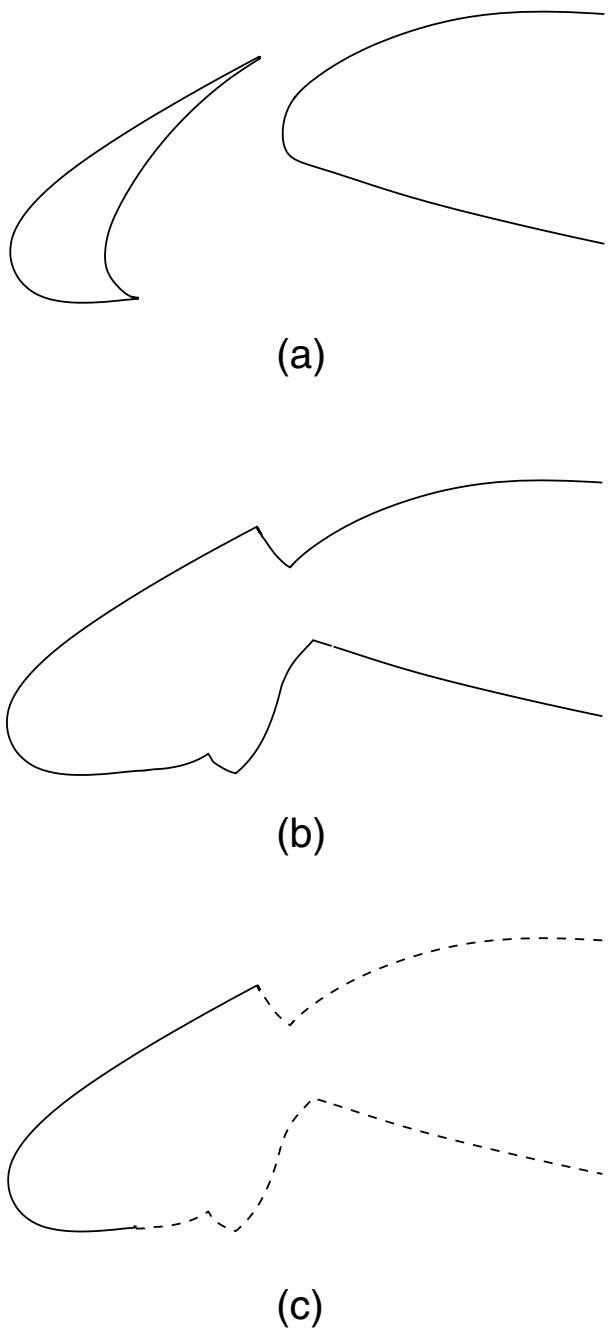

Figure 6. Data surfaces used for FW-H calculations. (a) On-body data surface. (b) Standard off-body data surface. (c) Modified off-body data surface (dashed line section is same as standard off-body data surface, solid line section is same as on-body data surface).

current Δt is four times larger than the time step used in reference 9. We chose a larger Δt to strike a balance between temporal resolution required for high-frequency trailing-edge vortex shedding and the need to generate a sufficiently long record to search for low-frequency shear-layer instabilities.

Figure 7(a-c) shows the instantaneous spanwise vorticity field in the slat vicinity for the forced case with the smaller frequency band. The three snapshots are sequential in time, with $1024\Delta t$ and $1408\Delta t$ separating the second frame from the first, and the third frame from the second, respectively. To put these separation times in perspective, using freestream velocity, approximate convective travel time from cusp to trailing edge is about $1400\Delta t$. Returning to figure 7, the most notable features in each snapshot are the formation of a free-shear layer due to boundary-layer separation at the slat cusp, and the presence of a strong vortex shedding at the blunt trailing edge. Vorticity contours clearly display the spatial location of the free-shear layer. Also, time evolution of the slat's shear layer is vividly apparent. Notice that the shear layer is a good amplifier of initial perturbations that result in a shear layer roll-up process and the formation of discrete vortices. Amplification of disturbances occurs via the well known Kelvin-Helmholtz (inflectional) instability mechanism.

Once formed, the vortices convect upward and impinge upon the slat undersurface at the reattachment point. Approaching the reattachment point, the vortices experience severe stretching and distortion due to rapid deceleration and subsequent acceleration of the local flow field. Vorticity plots also indicate that the large-scale structures disappear before reaching the slat trailing edge and no lumps of vorticity resembling a vortex escape through the gap.

Time-accurate simulation with the narrow-band (1,200 Hz $< f <$ 5,000 Hz) excitation confirmed our suspicions regarding the shear layer supporting large-scale unsteady structures. Therefore, starting from the same initial base flow, computation was repeated for the wider excitation band of 700 Hz $< f <$ 10,000 Hz. Both simulations, with exception of minor details, produce flow fields with similar features. Figures 8(a) and 8(b) provide a sample comparison between the computed spanwise vorticity field at the same instant in time. The shear-layer roll-up location and the size of the rollers are virtually the same, indicating nearly identical frequencies for the most amplified disturbances. Given the nearly identical states of the disturbed shear layer, for the remainder of this section only the computation obtained

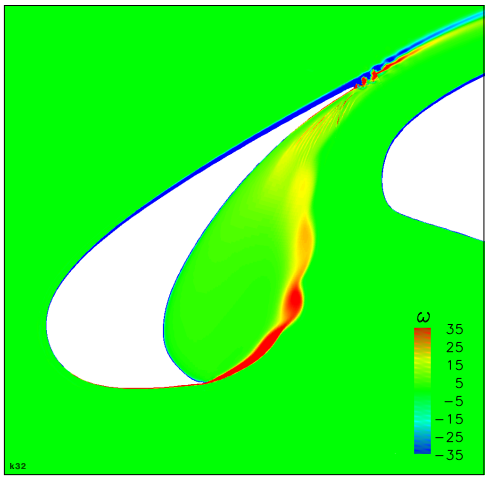

(a)

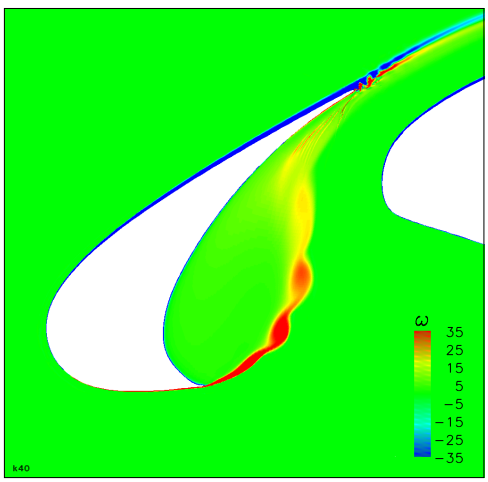

(b)

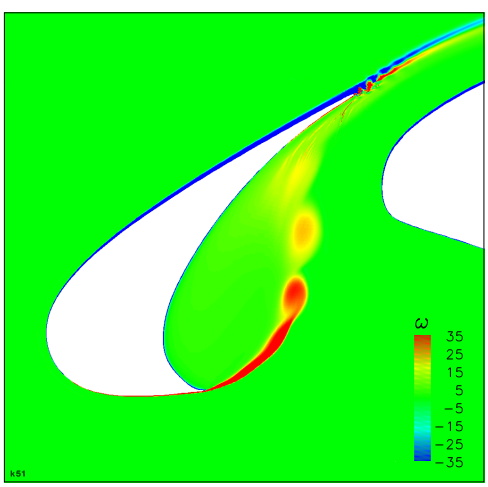

(c)

Figure 7. Simulated spanwise vorticity field for narrow bandwidth 3 percent forced case. (a) Early time. (b) Middle time. (c) Later time.

with the wider forcing band will be presented.

To determine shear-layer dominant modes of oscillation, several computational probes are placed within the computational domain in the slat's vicinity. Locations of the four primary probes used to ascertain time evolution of the shear layer are shown in figure 4. Probe 1 is closest to the slat cusp while probe 4 is situated near the shear-layer reattachment point. A sample record obtained from probe 3 inside the shear layer is plotted in figure 9. The prominent high-frequency oscillations are due to strong vortex shedding at the slat trailing edge. Each period in this frequency range includes about 35 time steps. The high-frequency signal is superimposed on much lower frequency oscillations caused by shear-layer instability. Based on the Fourier transform of the recorded time signals, the shear layer primary mode has a frequency that resides between 2,000 and 3,000 Hz.

Contrary to what one might expect, the recorded data does not indicate a continous roll-up process that results in the formation of a vortex chain; rather, it shows the process to be somewhat intermittent. For example, the time signal in figure 9 shows the passage of a large-scale structure close to $t = 6.7$, followed by a period of relatively lower amplitude oscillations followed by the passage of another vortex at $t = 7.2$. Scrutiny of the entire recorded signal in conjunction with the corresponding vorticity field failed to reveal a discernible pattern of a particular periodicity. At times, five or six vortices in a row are produced by the rolling-up of the shear layer followed by a period of low activity, while at other times only one or two vortices are formed. It must be pointed out however, that even during low-activity periods, low-frequency disturbances are still being amplified, producing weak undulations of the shear layer. Most likely, during these weak undulations the disturbances experience and undergo a linear growth stage without reaching the latter stages of non-linear growth and saturation states.

In order to present a more complete physical picture of disturbance evolution along the shear layer, unsteady signals from the four probes are considered simultaneously. Figure 10 displays the four individual time records Fourier transformed. Jaggedness of the tranformed signals is due to the combination of a) finiteness of the record, and b) discreteness of forced frequencies. Near the cusp (probe 1), the shear layer is thin and thus supports a wider frequency band of instabilities. Accordingly, we expect the fastest growing modes to have relatively high frequencies. The transformed signal from probe 1 sup-

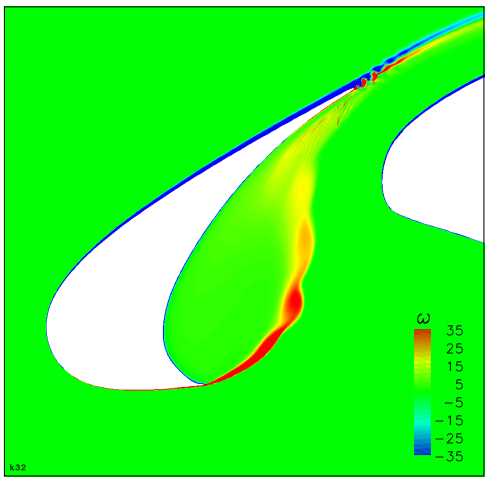

(a)

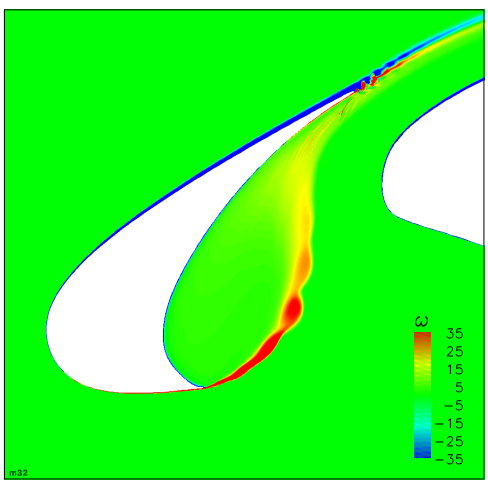

(b)

Figure 8. Comparison between spanwise vorticity fields. (a) Narrow-band excitation. (b) Wide-band excitation.

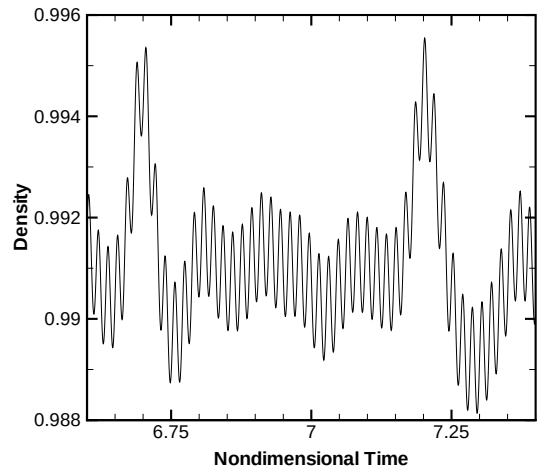

Figure 9. A sample time record from computational probe 3.

ports this claim and shows the most amplified disturbances are confined to the range 5,000 Hz $< f <$ 10,000 Hz. As the shear layer thickens downstream, the band of disturbances with the highest growth rates gradually shifts toward lower frequencies. Plotted signals from probe 2 and probe 3 clearly confirm this slow shifting of the amplified frequency band. By the time the shear-layer reattachment location (probe 4) is reached, high frequency perturbations are damped and primary amplified modes reside in the frequency band of 1,000 Hz $< f <$ 4,000 Hz. As a reminder, it is noted that the upper limit of 4,000 Hz agrees favorably with the slat's acoustic spectrum frequencies (see fig. 2) where amplitude drops off very rapidly. This agreement reinforces our opinion that flow unsteadiness supported by the shear layer is the mechanism responsible for the low-frequency content of the slat acoustic spectra.

Based on current and other recent studies, one may argue that an unsteady RANS simulation provides a useful tool for understanding complex flow-generated noise sources. Yet, as in the case of any computational methodology, there are some inherent defficiencies that deserve our comments before concluding the section. For the present set of simulations, a point of concern is the rapid dissipation of a rolled-up vortex (i.e., see fig. 7(c)). Also, the intermittency of the roll-up process may arguably result from this excessive dissipation. In present simulations, a typical roller is resolved with over 20 points along the stream and more than 40 points in normal directions. Thus, our spatial resolution of the cove region is fine enough to discard numerical vis-

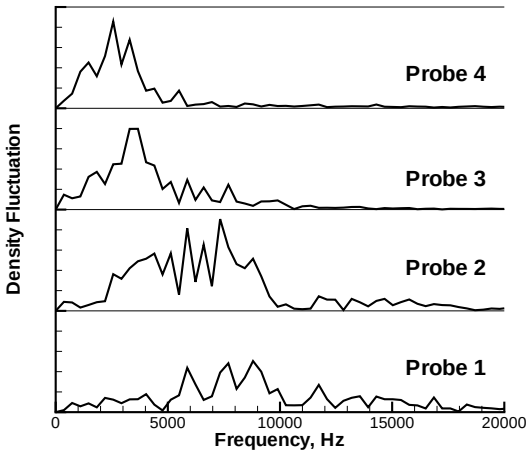

Figure 10. Fourier transforms of computational probe data.

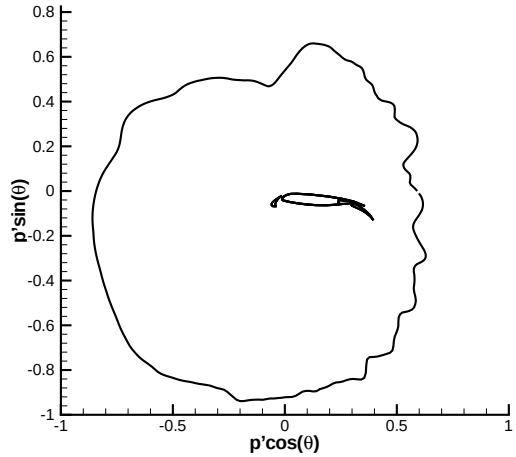

Figure 11. Far field noise directivity pattern.

cosity as a major contributor. We believe the only other factor with such first-order dissipative effects is the turbulence model. Most general purpose turbulence models are developed and calibrated for wall-bounded steady flow fields. The behavior of these models in an unsteady free-shear-flow is uncertain. We must reiterate however that our focus has been to uncover and highlight mechanisms responsible for slat noise. Issues concerning the turbulence model effects are beyond the scope of the present effort and deserve a thorough study of their own.

Acoustic Analysis

Figure 11 shows a directivity plot for the case in which a 3 percent wide-band forcing was applied. Only the energy in frequencies between 1,000 Hz and 20,000 Hz was used in computing directivity displayed here. The standard off-body data surface was used for the calculation. Noise preferentially propagates forward and downward, but the directivity plot does not contain significant strongly-directed lobes. Lack of strongly directed lobes is consistent with the broadband nature of the noise. Directivity plots that include narrower ranges of frequencies show more pronounced directivity sensitivity, mostly in the downstream direction (zero degrees). Because of the importance of the flyover direction (270 degrees) and the fact that the directivity in the vicinity of 270 degrees is not particularly sensitive to small changes in angle, all spectra reported below are taken at 270 degrees.

Figure 12 shows a comparison of the acoustic spectra obtained at 270 degrees for cases in which a 3 percent forcing was applied to 5,000 Hz (solid line) and 10,000 Hz (dashed line). For the case in which the forcing was applied to 10,000 Hz, spectra from four data segments were averaged to obtain the result shown. For the case in which forcing was applied to 5,000 Hz, only two data segments were available for averaging after the transient was removed. More data averaging would be desirable in both cases; however, even with the marginal data averaging, in both cases the sound pressure level (SPL) decreases significantly in the vicinity of respective maximum forcing frequencies. Strong decreases at these frequencies suggest that the sound radiated is strongly correlated to details of the forcing. Such strong correlation was not seen in spectra associated with the flow structures themselves (see fig. 10). For the acoustic data to be useful, we needed to understand why the acoustic field was more sensitive to forcing than the flow field.

One possibility for stronger sensitivity of the acoustics to forcing is that acoustic radiation might be dominated by acoustic scattering at the slat cusp. Because the slat cusp is only a small distance downstream of the forcing location, the effect of forcing might be expected higher right at the cusp than in the unstable shear layer. If acoustic scattering at the slat cusp were the reason for strong sensitivity in the acoustics to forcing, then use of the on-body data surface in the FW-H solver would give similar results to those obtained using the standard off-body data surface. In particular, the strong decrease in SPL around the maximum forcing frequency would be expected in both cases. Figure 13 shows a compari-

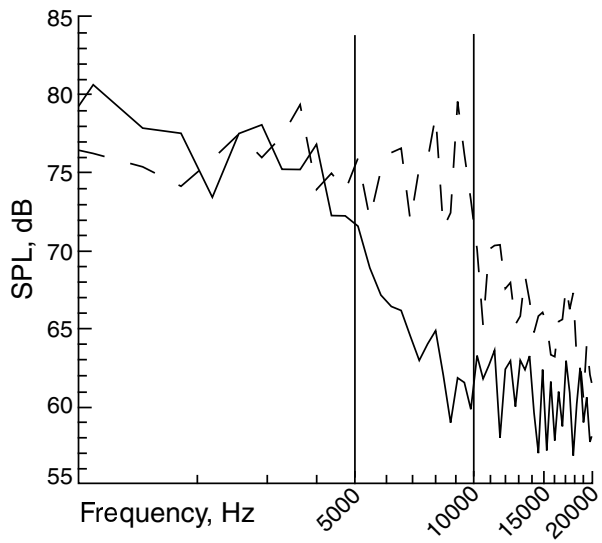

Figure 12. Far field noise spectra at 270 degrees for 3 percent forced cases. ——— forcing to 5,000 Hz, – – – – – forcing to 10,000 Hz. Vertical lines mark 5,000 and 10,000 Hz, reference pressure is 20μPa.

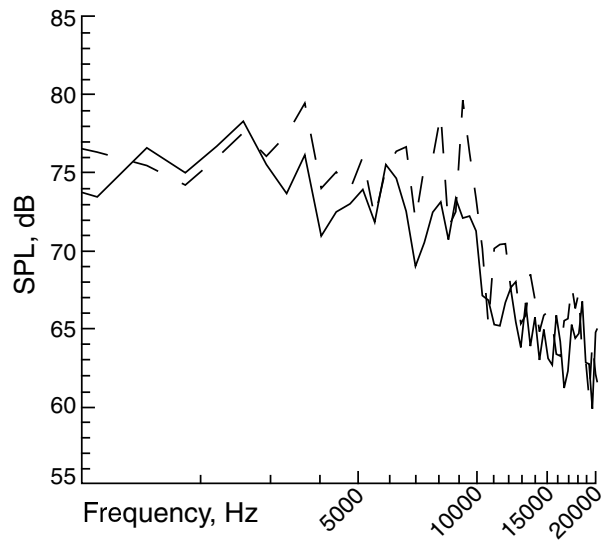

Figure 13. Far field noise spectra at 270 degrees for 3 percent forcing to 10,000 Hz. ——— On-body data surface, – – – – – standard off-body data surface, reference pressure is 20μPa.

son of the spectra at 270 degrees using the on-body data surface (solid line) and the standard off-body data surface (dashed line). In these calculations, flow velocity relative to the on-body data surface is assumed zero. The figure shows that the SPL starts to drop at a significantly lower frequency for the case in which the on-body data surface is used. A similar conclusion is reached for comparisions with the case in which forcing was stopped at 5,000 Hz. Acoustic scattering at the slat cusp was thereby ruled out as the source of the strong correlation between forcing and the acoustic spectrum.

Another set of FW-H calculations was performed with a data surface slightly dissimilar to the on-body data surface. Rather than being on the slat surface, the surface on the suction side of the slat was replaced by a surface that was just outside of the slat boundary layer. This very small displacement of the surface to outside the boundary layer was not expected to influence the acoustic results much. Surprisingly, the acoustic spectrum for this case was more similar to that obtained with the standard off-body data surface than with the on-body data surface.

The unpredicted behavior led to a desire to identify regions in which the right hand side of the FW-H equation (eq.(3)) was large. These would be the regions that would dominate the far-field radiation. Figure 14 includes contours of U_n from equation(3) in a point-index–frequency plane. The schematic in figure 14 shows the slat and main element bodies with dashed lines and the standard off-body data surface with a solid line. Leader lines show the correspondence of the various point indices to their locations on the off-body data surface. Although this figure only shows data for the case in which 3 percent forcing was applied to 10,000 Hz, the conclusions also apply to the case in which forcing was applied to 5,000 Hz.

The source term U_n is large in the 35,000 to 38000 Hz range, and vortex shedding at the slat's trailing edge dominates the source term at these high frequencies. This phenomenon and its acoustic impli-

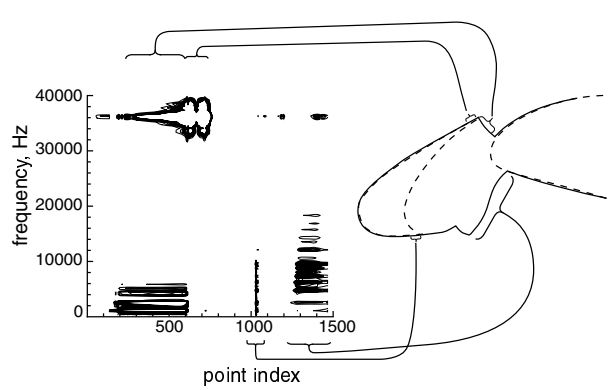

Figure 14. Contours of forcing term U_n as function of frequency and point position.

cations are reported in references 9 and 10. Source term U_n is also very strong in the 2,000 to 3,000 Hz range in the gap between the slat trailing edge and the main element. This large value is the result of acoustic radiation through the slat gap. This noise is most likely generated by flow structures associated with the shear-layer instabilities, probably as the flow structures interact with the slat.

Two other regions also show large values of U_n; both regions show that the source term is strong up to 10,000 Hz. One of these regions is a portion of the off-body surface stretching over a section of the cove. The other region is tightly clustered around the location at which forcing is applied. In retrospect, the U_n term should be large in the vicinity of the forcing. Forcing is applied as an oscillating mass flux through a small section of the slat. The oscillating mass flux directly contributes to source terms on the right-hand side of equation (3). The forcing is itself an acoustic source and direct radiation of that acoustic energy must be properly handled by the data surface. Neglecting diffraction effects, direct radiation of acoustic energy from forcing is expected to be most apparent on surfaces within a line-of-sight of the forcing region. This includes the small section directly below the forcing as well as the aft portion of the data surface that covers the cove. Because forcing contributes directly to acoustic radiation, we should not be surprised that far field acoustics includes a significant contribution from the forcing.

Recall that the spectrum obtained using the on-body data surface (fig.13) showed a significant decrease in acoustic energy at frequencies below 10,000 Hz. In retrospect, use of the zero-velocity condition on the entire slat surface was incorrect; forcing prescribes flow through the surface. The on-body data surface with zero surface velocity effectively filtered out much of the noise that would have been radiated directly from the forcing. Because the term L_i on the right-hand side of equation (3) is still nonzero, even with zero surface velocity the entire direct noise radiation from forcing is not removed.

To estimate what the acoustic radiation would be without forcing, we constructed the modified data surface shown in figure 6(c). It consists of the on-body data surface portion over the slat suction surface and the off-body data surface elsewhere. This modified data surface removes a portion of the direct acoustic radiation attributable to forcing and therefore provides a better representation of the acoustic radiation expected for a slat-cove shear layer excited by natural perturbations in the flow. The acoustic spectrum for the case with 3 percent forcing to

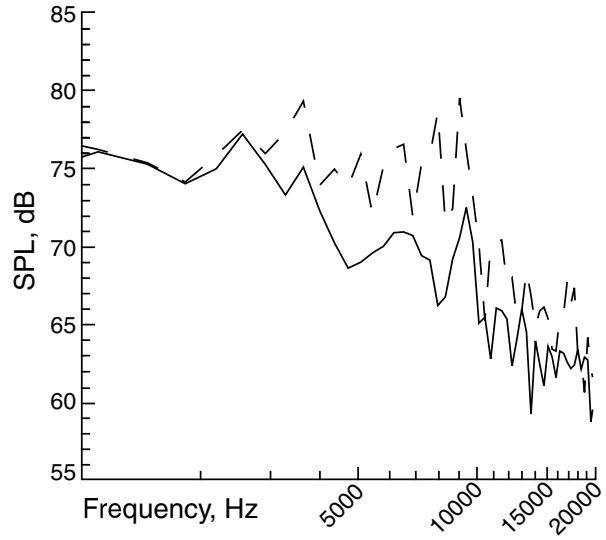

Figure 15. Far field noise spectra at 270 degrees for 3 percent forcing to 10,000 Hz. ——— modified off-body data surface, – – – – – standard off-body data surface, reference pressure is 20μPa.

10,000 Hz using the modified off-body data surface is compared with the results derived from using the standard off-body data surface (fig. 15). A significant decrease in acoustic energy occurs at frequencies between 4,000 Hz and 10,000 Hz.

Figure 16 compares the SPLs from the numerical simulations with experimental data. Because the experimental SPL was available only in $1/12^{th}$ octave, corresponding results from the numerical simulations have been transformed to $1/12^{th}$ octave. Here the experimental SPL values have been uniformly shifted downward by 25 dB. Such a large shift suggests that amplitudes computed in numerical simulations are significantly lower than those realized in practice. As elaborated in the previous section, lack of a proper amplitude may be attributed to premature dissipation of the large scale structures. Although a smaller shift would have been desirable, the important point is that the decrease in SPL occurs at approximately the same frequency in both the experiment and the simulation. This fact strongly suggests that numerical simulations are capturing the basic physical mechanisms responsible for the noise.

Conclusions

Time-accurate RANS simulations on a fine grid were used to identify the sources of flow unsteadiness in a slat's cove region. Formation and subsequent development of the free shear-layer near

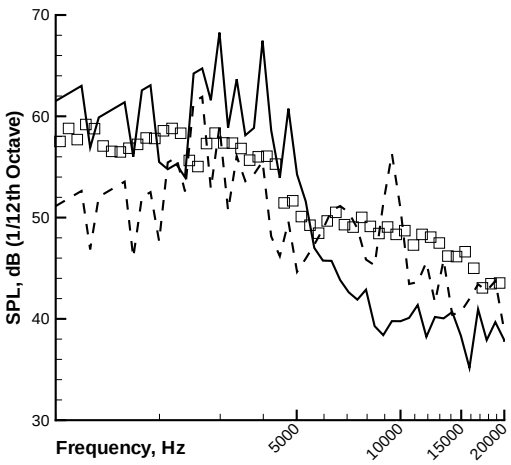

Figure 16. Far field noise spectra at 270 degrees with modified off-body data surface with ——— 3 percent forcing to 5,000 Hz, – – – – – 3 percent forcing to 10,000 Hz, ▫ experimental data downward shifted by 25 dB. SPL data is $1/12^{th}$ octave with reference pressure of 20μPa.

the cusp was accurately captured. Initial computations were conducted without forcing. These calculations suggested that the shear layer supports low frequency oscillations. To better isolate the unsteady mechanism(s), subsequent simulations involved forcing of the shear layer on the slat surface near the cusp. Simulations obtained with narrow-frequency and wide-frequency excitation bands produced nearly identical final states. Analysis of the computational database revealed the shear layer underwent and maintained large scale flow oscillations. Amplification of the initial forcing field was achieved via the Kelvin-Helmholtz (inflectional) instability mechanism, resulting in the shear-layer roll-up process and formation of discrete vortices. The amplified disturbances resided in the frequency band 1,000 Hz $< f <$ 4,000 Hz, corresponding to the band of frequencies with large amplitudes in the slat's acoustic spectra. Once formed, the discrete vortices underwent severe distortion as they approached the shear-layer reattachment point on the slat underside surface. Beyond the reattachment point, the vortices disintegrated and virtually disappeared before reaching the slat trailing edge. For the angle of attack considered, no vortex was observed to escape through the slat gap.

The far field noise was computed by solving the Ffwocs Williams and Hawkings equation with a permeable data surface. Flow from the unsteady RANS calculations was used to provide the necessary information on the data surface. Only the surface terms were included in the computation. Preliminary computations of the acoustic field suggested that the imposed forcing used to excite the instabilities dominated the acoustic field. Additional calculations, using a variety of data surfaces, revealed that direct acoustic radiation associated with the imposed forcing accounted for much of the observed noise. A significant portion of the direct radiation was eliminated by use of a data surface that coincided with the slat body in the region of imposed forcing. The resultant acoustic spectrum has a broad peak in the 3,000 Hz range, similar to what is seen in the experimental data. Although amplitude of the computed noise is much less than what was measured, the spectrum shape in the mid-frequency range is similar. This similarity strongly suggests that growth of vortices in the shear layer is largely responsible for radiated noise in this frequency range.

Acknowledgments

Work of the first and third authors was partially sponsored by NASA contract NAS1-20102 (Lockheed Martin Corporation subcontract RT46324) while working at High Technology Corporation. The majority of the simulations were performed on the C-90 Cray computers provided by the National Aerodynamic Simulation (NAS) Facility. The authors have greatly benefited from interactions with members of the Airframe Noise Team at NASA Langley Reaserch Center. In particular, many useful discussions with Drs. Meelan Choudhari, Craig Streett, and David Lockard are gratefully acknowledged.

References

1. Macaraeg, M. G., "Fundamental Investigations of Airframe Noise," AIAA Paper No. 98-2224, 1998.

2. Hayes, J. A., Horne, W. C., Soderman, P. T., and Bent, P. H., "Airframe Noise Characteristics of a 4.7% Scale DC-10 Model," AIAA Paper No. 97-1594, 1997.

3. Dobrzynski, W., Nagakura, K., Gehlhar, B., and Buschbaum, A., "Airframe Noise Studies on Wings with Deployed High-Lift Devices," AIAA Paper No. 98-2337, June 1998.

4. Davy, R.and Remy, H., "Airframe Noise Characteristics on a 1/11 Scale Airbus Model," AIAA Paper No. 98-2335, June 1998.

5. Grosche, F.-R., Schneider, G., and Stiewitt, H., "Wind Tunnel Experiments on Airframe Noise

Sources of Transport Aircraft," AIAA Paper No. 97-1642, 1997.

6. Michel, U., Barsikow, B., Helbig, J.and Hellmig, M., and Schuttpelz, M., "Flyover Noise Measurements on Landing Aircraft with a Microphone Array," AIAA Paper No. 98-2336, 1998.

7. Storms, B. L., Hayes, J. A., Moriarty, P. J., and Ross, J. C., "Aeroacoustic Measurements of Slat Noise on a Three-Dimensional High-Lift System," AIAA Paper No. 99-1957, 1999.

8. Olson, S., Thomas, F. O., and Nelson, R. C., "A Preliminary Investigation into Slat Noise Production Mechanisms in a High-Lift Configuration," AIAA Paper No. 2000-4508, 2000.

9. Khorrami, M. R., Berkman, M. E., and Choudhari, M., "Unsteady Flow Computations of a Slat with a Blunt Trailing Edge," *AIAA Journal*, Vol. 38, No. 11, November 2000, pp. 2050–2058.

10. Singer, B. A., Lockard, D. L., and Brentner, K. S., "Computational Acoustic Analysis of Slat Trailing-Edge Flow," *AIAA Journal*, Vol. 38, No. 9, September 2000, pp. 1558–1564.

11. Paschal, K., Jenkins, L., and Yao, C., "Unsteady Slat Wake Characteristics of a 2-D High-Lift Configuration," AIAA Paper No. 2000-0139, 2000.

12. Takeda, K., Ashcroft, G. B., and Zhang, X., "Unsteady Aerodynamics of Slat Cove Flow in a High-Lift Device Configuration," AIAA Paper No. 2001-0706, 2001.

13. Menter, F., "Improved Two-Equation k-ω Turbulence Models for Aerodynamic Flows," NASA TM 103975, 1992.

14. Singer, B. A., Brentner, S., K., Lockard, D. L., and Lilley, G. M., "Simulation of Acoustic Scattering from a Trailing Edge," *Journal of Sound and Vibration*, Vol. 230, No. 3, February 2000, pp. 541–560.

15. Ffowcs Williams, J. E. and Hawkings, D. L., "Sound Generated by Turbulence and Surfaces in Arbitrary Motion," *Philosophical Transactions of the Royal Society*, Vol. A264, No. 1151, 1969, pp. 321–342.

16. Brentner, K. S. and Farassat, F., "An Analytical Comparison of the Acoustic Analogy and Kirchhoff Formulation for Moving Surfaces," *AIAA Journal*, Vol. 36, No. 8, 1998, pp. 1379–1386.

17. Lockard, D. P., "An Efficient, Two-Dimensional Implementation of the Ffowcs Williams and Hawkings Equation," *Journal of Sound and Vibration*, Vol. 229, No. 4, 2000, pp. 897–911.